Article:
Sun, B, Zhang, Q, Xiang, H et al. (7 more authors) (2020) Enhanced active sulfur in soft carbon via synergistic doping effect for ultra–stable lithium–ion batteries. Energy Storage Materials, 24. pp. 450-457. ISSN 2405-8297

https://doi.org/10.1016/j.ensm.2019.07.014

Enhanced Active Sulfur in Soft Carbon via Synergistic Doping Effect for Ultra–stable Lithium–ion Batteries

Bing Sun[a], *Qin Zhang*[a,*], *Hui Xiang*[a], *Fei Han*[b], *Wen Tang*[a], *Guanming Yuan*[a], *Ye Cong*[a], *Changling Fan*[b], *Aidan Westwood*[c], *Xuanke Li*[a, b,**]

[a] The State Key Laboratory of Refractories and Metallurgy, Wuhan University of Science and Technology, Wuhan 430081, China

[b] Hunan Province Key Laboratory for Advanced Carbon Materials and *Applied Technology*, Hunan University, Changsha 410082, China

[c] School of Chemical and Process Engineering, University of Leeds, Leeds, LS2 9JT, United Kingdom

Graphical Abstract:

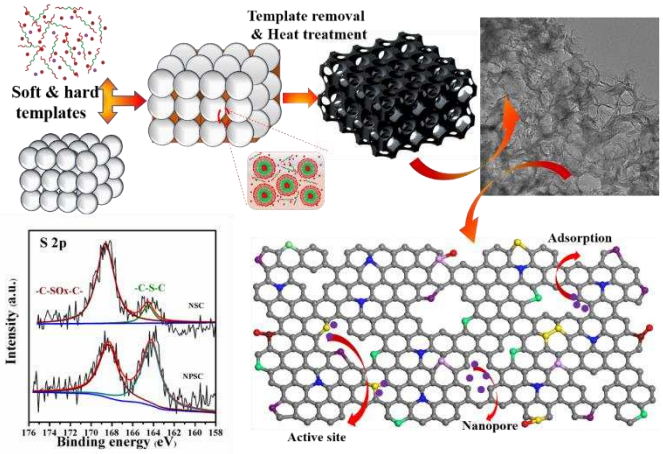

Based on a combined soft–hard templates method, N, P and S ternary–doped hierarchical porous soft carbon (NPSC) was prepared from mesophase pitch via a one–pot reaction. It was found that the introduction of P promotes the incorporation of sulfur into carbon rings by formation of C–S bonds. The increased interlayer spacing and synergistic doping effect among various heteroatoms provide a rapid transport pathway for ions, and hence faster reaction kinetics, and more Li^+ storage active sites.

*Corresponding author. E–mail addresses: zhangqin627@wust.edu.cn (Q. Zhang);
**Corresponding author. E–mail addresses: xkli8524@sina.com (X.K. Li).

Abstract

The formation of C–S bonds with high activity in a carbon skeleton is considered to be one of the most effective strategies to facilitate highly reversible alkali storage reactions. In this work, by the combination of heteroatomic control and structural design, N, P and S ternary–doped hierarchical porous soft carbon (NPSC) is obtained with a high concentration of C–S bonds, large specific surface area and large graphitic interlayer spacing. As anode materials for lithium–ion batteries (LIBs), NPSC exhibits a reversible capacity of 500 mA h g^{-1} and 90% capacity retention can be realized at 500 mA g^{-1} after 500 cycles, showing its high–rate capability and long–term cyclability. In addition, a full cell based on a $LiVPO_4F$ cathode and an NPSC anode delivers high discharge capacity and superior cycling stability. This high performance is attributed to the introduction of P, which promotes the utilization of S through the formation of C–S bonds. In addition, the synergistic doping effect increases the interlayer spacing, facilitating rapid interfacial Li^+ adsorption and diffusion reactions. This strategy provides an efficient route toward excellent heteroatom–doped carbon for energy storage and conversion applications.

Keywords:
synergistic doping effect; increased interlayer spacing; C–S bonds; soft carbon; adsorption energy.

1. Introduction

Emissions of carbon dioxide and other greenhouse gases increase the global average surface air temperature and hence routes to clean energy are attracting increasing attention at present [1] . Lithium–ion batteries (LIBs) offer overwhelming advantages and are considered to be indispensable for the development of renewable energy−powered devices [2, 3]. Soft carbon, with its high abundance and controllable crystallinity, can be widely applied as the anode material in LIBs. In addition, soft carbon with suitable combinations of structural order and disorder offers good compatibility with electrolyte and this is favorable for the electrochemical stability. However, soft carbon still suffers from the issue of poor conductivity and low Li^+ diffusion rate [4–7]. To solve this issue, modification by N−doping and architectural design of soft carbon have been widely investigated, leading to better lithium storage performance. On one hand, N−doping can enhance the electronic conductivity of carbon and generate more active sites in carbon frameworks, and on the other hand, the mesoporous structure shortens the path for ion diffusion and facilitates the penetration of electrolytes [8−14].

To further improve the performance of N−doped soft carbon, multiple heteroatom (such as S as well as N) doping into the carbon framework was considered to be an efficient method due to a synergistic doping effect. For instance, N, S doped carbon materials have been proved to exhibit better electrochemical performance than that of solely N−doped carbon [15−23]. This arises from S atoms with larger covalent radius which can alter the electronic and metallic properties of N−doped soft carbon. Moreover, at defect sites, the C−S bonds in N, S−doped carbon materials can give rise to an obvious torsion of carbon layer. As a result, the interlayer spacing is enlarged and this facilitates the easy insertion of Li^+ ions during charging. Nevertheless, during the sulfidation process, most S atoms tend to exist in the form of oxidized sulfur which possesses low reactivity and exhibits low utilization during lithiation process [24−26]. Hence, a sharp increase in C−S bonds concentration could enable N, S−doped soft carbon to exhibit highly reversible lithium storage performance, and this needs further exploration.

Here, we employ a facile method to prepare N, P, and S co–doped soft carbon (NPSC), derived from mesophase pitch. The introduction of P can be expected to promote the formation of C–S bonds, which provide more storage sites and enlarge the interlayer spacing. Additionally P doping, with lower electronegativity than that of N or S, can also modify the electronic properties and accelerate electron transfer, leading to an increasing partial reactivity. In line with expectations, the as–prepared NPSC shows a reversible capacity of 650 mA h g^{-1} at 100 mA g^{-1} after 100 cycles and exhibits ultra–stable cycle performance for LIBs up to 500 cycles with negligible capacity fading at a current density of 0.5 A g^{-1}. Moreover, the multi–atoms doping can result in a larger asymmetric spin and higher charge density on active carbon atoms, thereby further improving the electronic conductivity of soft carbon. Therefore, this strategy can provide an efficient route toward excellent heteroatom–doped carbon for energy storage applications.

2. Experimental

All the chemicals used in this work were obtained without further purification and are commercially available unless otherwise stated.

2.1. Synthesis of N, P, and S co–doped carbon (NPSC)

The porous carbon was produced via a nanocasting path using nano–$CaCO_3$ and poly (propylene glycol)–block–poly (ethylene glycol)–block–poly (propylene glycol) (F127) as the hard and soft templates, respectively. Mesophase pitch (MP) was used as the carbon precursor (The typical properties and elemental analysis were listed in Table S1 and S2). During the preparation process, MP was mixed with tetrahydrofuran (THF) in a closed vessel with a mass ratio of 1:4. The mixture was first ultrasonicated for 20 min and then vibrated vigorously for 48 h. The resulting dispersion was filtered to remove the insoluble portion, yielding a concentrated precursor solution of MP.

In a typical experiment, an aliquot of solution that contains 1 g of MP, 0.5 g of F127, and 3.5 g of nano–$CaCO_3$ was put into a closed vessel under vigorously stirring for 12 h; then 0.3 g of melamine, 0.1 g of sulfur and 0.1 g of amorphous phosphorus were added into the as–prepared solution. The resultant mixture was continuously stirred until evaporation of the solvent was complete. The resulting powders were then dried overnight at 80 °C in air.

This as–prepared precursor was heated at 350 °C for 2 h, then carbonized at 800 °C for 2 h with a heating rate of 5 °C/min in a tubular furnace under a flowing nitrogen

atmosphere. The powders prepared in this way were treated with diluted hydrochloric acid for 2 days, then centrifuged and washed with water to remove templates $CaCO_3$ particles. After a freeze–drying process, NPSC with porous structure was obtained.

2.2. Synthesis of N doped carbon (NC), N and P codoped carbon (NPC), or N and S codoped carbon (NSC)

All samples for controlled trials were prepared via similar steps to those used for the synthesis of NPSC but using different precursors. NC was obtained by pyrolysis of MP and melamine. NPC was prepared by heating a mixture of MP, melamine and phosphorus. NSC was synthesized by heating a mixture of MP, melamine and sulfur. The heating conditions were the same as above. All as–prepared products were kept intact and collected before characterization and further use.

2.3. Material characterization

Crystallinity data for the samples was obtained by powder X–ray diffraction (XRD) (Bruker D8 venture) with Cu K_α radiation. Raman spectra were obtained by using a Lab RAM HR UV/vis/NIR with an excitation laser beam wavelength of 532 nm. Scanning electron microscope (SEM) images were obtained using a JEOL JSM–6701F scanning microscope at an accelerating voltage of 20 kV. Transmission electron microscope (TEM) characterization was conducted using a JEM–2100 (JEOL Ltd, Japan) with an accelerating voltage of 200 kV, attached to an energy dispersive X–ray spectrometer (EDX) to obtain elemental mapping. The specific surface areas were measured by the Brunauer–Emmett–Teller (BET, Autosorb IQ) method based on the N_2 adsorption. The pore size distributions were calculated from adsorption data of isotherms using Barrett–Joyner–Halenda (BJH) method. The current−voltage (I−V) curves were obtained on an electrochemical workstation (CHI660D) using the compressed pellets (100 mg) of 13 mm in diameter, which are pressed in a stainless−steel mold by using 10 MPa pressure. X–ray photoelectron spectroscopic (XPS) measurements were carried out on a Thermo Fisher K–Alpha 1063 instrument using an Al K_α source, and the C 1s peak at 284.5 eV was taken as the internal standard. Elemental analysis (EA) was performed using an Elementar Vario MICRO cube analyzer in order to obtain the bulk composition.

2.4. Electrode preparation and electrochemical experiments

Electrochemical measurements were performed using CR2016 coin–type cells assembled in an Argon–filled glove box with oxygen and water contents less than 0.1 ppm. The working electrodes were prepared from a mixture containing the active

material under test, Super P and polyvinylidene fluoride (PVDF) with a weight ratio of 8:1:1 in 1–methyl–2–pyrrolidinone (NMP) solvent. The geometric area and mass of the working electrode were ca.1.54 cm^2 and 2.5–3.0 mg, respectively. Lithium metal and microporous polypropylene film (Celgard 2400) were used as the counter/reference electrode and separator, and 1 M $LiPF_6$ in ethylene carbonate (EC)/dimethyl carbonate (DMC) (1:1 by volume) with 5% fluoroethylene carbonate (FEC) was used as the electrolyte and the electrolyte amount is 400 μL per coin cell.

Galvanostatic charge–discharge tests of the electrodes were carried out at various current densities ranging from 0.005 V to 3 V using a battery test system (Land CT2001A) at 30 °C. Cyclic voltammetry (CV) experiments were carried out using an electrochemical workstation (CHI660D) at a sweeping rate of 0.1 mV s^{-1} in the same potential range as the charge/discharge process. Electrochemical impedance spectroscopy (EIS) measurements were conducted on a Gamary–1000E electrochemical workstation from 0.01 Hz to 100 kHz.

2.5. Computational methods

Density functional theory (DFT) calculations were performed using the Vienna Ab–initio Simulation Package (VASP) code. A generalized gradient approximation (GGA) to the exchange–correlation functional of Perdew–Burke–Ernzernhof (PBE) was applied. The polarization p–function (DNP) was chosen as the basis set for the augmented double numerical atomic orbital. The Brillouin Zone sampling used was 5 × 5 × 1 in the Monkhorst–Pack grid; the vacuums thickness was 25 Å and a plane–wave energy cutoff of 550 eV was employed for all computations [27, 28].

The adsorption energy (E_{ad}) is defined as $E_{ad} = E_{Li/support} - E_{Li} - E_{support}$, where $E_{Li/support}$, E_{Li} and $E_{support}$ are for the support with Li, the total energies of free Li and the corresponding support, respectively. With this definition, a negative value indicates an exothermic adsorption. The same periodic box dimensions and the same level of calculations are used to obtain all the energies, *i.e.*, $E_{adsorbate}$, $E_{support}$, and $E_{adsorbate/support}$.

3. Results and discussion

A schematic illustration demonstrates the preparation process for a heteroatom–doped hierarchical porous soft carbon framework for rechargeable LIBs (Fig. S1). As illustrated, the hierarchical porous soft carbon is fabricated via F127 and nano–$CaCO_3$ serving as templates and THF as solvent. Both F127 and mesophase pitch (Fig. S2b and

S2c) exhibited a high dissolution in the THF, whose surface tension reducing effect on $CaCO_3$ particles ensured a good dispersion. After a self–assembly process, the uniformly dispersed F127 coalesced into larger aggregates, which are primarily mediated by the Van der Waals interactions and the hydrogen bonds between F127 molecules and an organic precursor[29, 30]. Then, with the introduction of $CaCO_3$ particles and doping agents, the as–prepared aggregates impregnate into the porous structure of these hard templates. This was followed by a high temperature pyrolysis and carbonization process, and the sublimed and gasified sulfur and amorphous phosphorus diffused into the resulting carbon skeleton and then substituted a very small proportion of carbon atoms. As a consequence, hierarchical porous soft carbon with homogeneous doping was obtained after the heat treatment and template removal procedures. Schematic illustration of lithium intercalation in hierarchical porous soft carbon with homogeneous doping was shown in Scheme 1.

The morphology of the as–prepared doped porous carbon was characterized by SEM. Fig. 1a–d show the highly porous 3D hierarchical network and interconnected mesopore structure corresponding to the NC, NSC, NPC and NPSC, in contrast with the soft carbon without templates and dopants (Fig. S2a). Moreover, a large area of twisted thin graphene–like sheets can be clearly observed on the surface of NPSC.

The BET surface area of the corresponding doped carbon materials is measured via N_2 adsorption–desorption isotherm (Fig. S3). As can be seen clearly from the figures, the observed isotherms show typical type IV isotherms, indicating the mesoporous characteristics of these carbon samples. The specific surface areas of NPSC, NPC, NSC and NC are 163.1, 132.7, 125.8 and 113.5 $m^2 g^{-1}$, respectively. With the introduction of S and P, the specific surface area of porous carbon increases from 113.5 $m^2 g^{-1}$ to 163.1 $m^2 g^{-1}$, while the total pore volume increases slightly (Table S3). The pore size distribution shown in the inset of Fig. 1a–d suggest a large amount of mesopores of diameters around 3~7 nm, 10~20 nm and 35~50 nm which can provide numerous interpenetrating channels to allow effective infiltration of electrolyte into the electrode materials and shorten the distance of Li^+ transport.

The structure of the as–synthesized heteroatom–doped soft carbon was further analyzed by XRD and Raman spectra. As shown in Fig. S4, the XRD patterns of obtained products all exhibit similar diffraction features with a broad peak centered at

25.7°, corresponding to the (002) plane of the disordered carbon structure. Meanwhile, the (002) peak gradually shifts to a lower angle that varies with the doping of N, P and S, indicating the increased interlayer spacings. The heteroatom–doped soft carbon materials exhibit larger d_{002} spacings than that of graphite. The increased interlayer spacing is favorable for the highly reversible Li^+ insertion/extraction due to its lower transfer resistance. The Raman spectra of the as–synthesized porous carbon materials (Fig. 1e) show two prominent peaks around 1341 and 1592 cm^{-1}, corresponding to the disorder in the sp^2–hybridized carbon (D band) and the stretching vibration of unsaturated carbon (G band), respectively. The intensity ratio of these two bands (I_D/I_G) can reflect the graphitization degree of carbon materials [31]. NPSC demonstrated the highest intensity ratio (I_D/I_G=1.165) compared with that of NPC (I_D/I_G=1.147), NSC (I_D/I_G=1.143) and NC (I_D/I_G=1.121). The results indicate that a synergistic doping effect in the hierarchical porous carbon framework leads to the formation of defects during the preparation process, which mainly depends on the various atomic radii of doping elements (S 1.04 Å, P 1.10 Å and N 0.74 Å) and the contrast in valence states between heteroatoms and carbon. Meanwhile, the introduction of heteroatoms into the carbon network and the effect of templates result in the formation of curved carbon layers and a local geometrical distortion in the carbon network, thus hindering the formation of an ordered carbon structure [32]. The structurally amorphous character of NPSC is in good agreement with the results of the XRD shown in Fig. S4.

The chemical composition and surface electronic state of the heteroatom–doped soft carbon were investigated by EA and XPS. The elemental contents of the bulk materials measured by EA are listed in Table S4, revealing that the contents of C, N and S in NPSC are 74.64wt%, 5.50wt% and 3.65wt%, respectively. However, the doping concentrations of N, S and P as measured by XPS are 9.60at%, 0.95at% and 0.65at% (Table S5), respectively, revealing the existence of S and P in the N–doped carbon. Therefore, on an at% basis, EA indicates a N:S ratio of ca. 3.4 to 1, whereas XPS indicates a corresponding ratio of ca. 10.1 to 1, suggesting that nitrogen preferentially occupies surface sites, in comparison with sulfur. The full spectrum of NPSC (Fig. S5) confirms five characteristic peaks, attributed to C 1s, N 1s, S 2p, P 2p and O 1s spectra. For NC, only C 1s, N 1s, and O 1s peaks emerge in survey spectra. After S and P doping, two new peaks at 164 and 133 eV are attributed to S 2p and P 2p, respectively, confirming the successfully doping of S and P into the porous carbon network. In

addition, the C1s peak of NPSC are shown in the Fig. S6, and this is fitted to several individual peaks: C–C bonds (284.5eV), C–S bonds (284 eV), C–P/C–O or C=N bonds (285.2 eV), C=O or C–N bonds (286.5 eV) and O–C=O bonds (289 eV) [33, 34]. As shown in Fig. S7 and Table S6, the XPS–N1s peak of the prepared carbon can be fitted to contributions from four kinds of N species; peaks at around 398.6, 399.4, 400.4, and 404.3 eV corresponding to pyridinic nitrogen, pyrrolic nitrogen, graphitic nitrogen, and pyridinic N^+–O–, respectively [35]. The content of pyridinic N, pyrrolic N and graphitic N in NPSC are the highest among all of the samples, and this contributes to NPSC's excellent conductivity and good rate performance in lithium ion storage. The XPS spectra of the P–doped carbons are shown in Fig. 1f. The P 2p state exhibits two typical peaks centered at 133.0 eV and 134.6 eV, which can be ascribed to P–C and P–O bonding, respectively. With the doping of S atoms, the peak position of P–O shifts to lower binding energy, and another new peak appears at 133.8 eV, indicating the presence of P–S bonds [36]. As reported, theoretical calculations show that P–doping in carbon induces the negatively delocalization of C atoms adjacent to P atoms, due to the fact of lower electronegativity of P (2.19) than that of C (2.55) and thus results in a negative charge around the carbon atoms which can reinforce the adsorption interaction with Li^+ [37, 38]. The S 2p peak is split into two peaks at 164.5 and 168.6 eV, corresponding to the binding energies of sulphide (C–S–C/S–P) and sulphone (C–SO_x–C), respectively. The comparison between the binding energies of sulphide and sulphone in NSC and NPSC are illustrated in Fig. 1g. Notably, when there is P doping, the peak centered at 168.6 eV exhibits an obvious decrease in intensity, accompanied by an enhancement in intensity of the peak at 164.5 eV; the relative proportion of C–S–C increases by 40.82% , indicating that the majority of the doped S atoms are in the form of non–oxidized states in the carbon, which could introduce more electrons to the π–conjugated system of carbon, and thus improve the electrochemical activity of anode material as well as offer more active sites when used for LIBs.

Furthermore, the synergistic doping effect on the microstructure of heteroatom–doped soft carbon was demonstrated by TEM. Fig. 2a confirms the existence of abundant mesopores and sheet–like structure in NPSC. The inset in Fig. 2a is the selected area electron diffraction (SAED) pattern of NPSC. It indicates that the amorphous character of heteroatom–doped soft carbon is in accordance with the high–resolution TEM image (Fig. 2b) in which turbostratic carbon layers are visible. This

HRTEM image of NPSC shows that the soft carbon is composed of both ordered and disordered carbon layers which offer benefits in terms of the electronic conductivity and the penetration of electrolyte, respectively. The increased interlayer spacing (d_{002}) in NPSC (magnified and inset in Fig. 2(b)) is 0.372 nm – larger than that of NPC (0.359 nm), NSC (0.354 nm) and NC (0.342 nm) (Fig. S8) and this offers benefits in terms of Li^+ intercalation/deintercalation. Furthermore, TEM elemental maps of NPSC shown in Fig. 2c and 2d reveal the uniform distribution of N, P and S throughout the carbon framework.

The current–voltage (I–V) curves of the wafers made from the as–prepared various carbon materials are shown in Fig. S9. Among all the samples, NPSC and NC manifest the highest and the lowest electronic conductivities, respectively. This indicates that N, P and S co–doping can significantly improve the electronic conductivity of carbon materials for use as anodes. NPC (with a P concentration of 0.84at% and a N concentration of 8.85at%) delivers higher conductivity in comparison with NSC (with a S concentration of 0.80at% and a N concentration of 10.78at%), indicating that the P doping contributes a larger enhancement to the electronic conductivity of the as–prepared soft carbon than S doping does. Previously theoretical calculations have demonstrated that P and/or S doping is able to improve the electron–donor properties of carbon materials, conclusively accompanied by an increased conductivity, and this is consistent with our results [25, 38].

To evaluate NPSC's superior electrochemical properties, NPSC electrodes were directly investigated using a half–cell configuration versus Li metal. Cyclic voltammetry (CV), galvanostatic charge/discharge (GCD), rate capacity and cycle retention measurements were performed. Fig. 3a and Fig. S10 show the initial five CV curves of electrode materials in the range of 0.005~3 V (vs Li/Li^+) at a scan rate of 0.1 mV s^{-1}. There exists an oxidation peak in the potential range of 1.0~0.005 V in the first cathodic scan, which could be ascribed to the decomposition of electrolyte and the formation of a solid electrolyte interface (SEI) film on the electrode surface [39, 40]. The lithium insertion/deintercalation potentials are around 0 V and 0.2 V vs. Li/Li^+. Notably, the CV curves almost overlap after the first cycle except that the current intensity in the range of 0.5~0.005 V decreases slightly, indicating the relative stability of the electrode and the reversibility of the electrochemical reactions. Fig. 3b presents the charge/discharge profiles of the NPSC electrode in the 1st, 2nd, 10th, 30th, 50th and

100th cycles at a current density of 100 mA g^{-1} between 0.005~3 V for LIBs. NPSC delivers an initial discharge capacity of 1239.8 mA h g^{-1} and a restorable charge capacity of 770 mA h g^{-1}. In addition to conventional Li^+ intercalation, the 3D porous structure also contributes to extra lithium storage, while the open edge sites created by heteroatom–doping ensures a relatively higher capacity of the materials. The initial coulombic efficiency is measured to be 62.1% and the irreversible capacity loss could be attributed to the formation of SEI film caused by reduction of the electrolyte and irreversible Li^+ insertion into special positions in the vicinity of residual H atoms during the first cycle [41], which is consistent with CV plots. The cycling performances of the as–prepared materials were evaluated by GCD measurements at a current density of 100 mA g^{-1} and the capacity decreases slightly in the first 10 cycles and then gradually stabilizes（Fig. 3c）. After slow fading in the initial 10 cycles, NPSC delivers a stable reversible capacity of 650 mA h g^{-1} with nearly 99.9% coulombic efficiency. Moreover, the reversible capacities of NPS, NSC and NC after 100 cycles are maintained at about 508.7, 481.1 and 346.9 mA h g^{-1}, respectively. The specific data is shown in Table S7. Obviously, NPSC exhibits a higher reversible capacity than the other materials due to its N, P and S co–doping. Owing to the synergistic effect of its heteroatoms, NPSC possesses an excellent electrical conductivity and a high content of C–S bonds offering more active sites for Li^+.

It is certain that the synergistic doping effect of heteroatoms is favorable for the insertion/extraction of Li^+ into/out of carbon layers due to the larger interlayer spacing and more active sites, especially in terms of the rate performance. To verify this, the rate performance of the prepared anode at various current densities was measured and these are displayed in Fig. 3d. Reversible capacities of 668, 596, 500, 406 and 305 mA h g^{-1} were obtained at 100, 200, 500, 1000 and 2000 mA g^{-1}, respectively. When the current density is adjusted back to 100 mA g^{-1}, the reversible capacity recovers to a value of 635 mA h g^{-1}. NPSC shows outstanding cycling performance and rate capacity, which are superior to other samples. To further elucidate its remarkable cycling stability at high current densities, after the test of rate performance, the cell was evaluated at a current density of 500 mA g^{-1} for long–term cycling. As shown in Fig. 3e, the capacity is maintained at 489.5 mA h g^{-1} even after 500 cycles and the coulombic efficiency is near 100%. Compared with reported carbonaceous or heteroatoms doped carbon materials (Table S8), N, P and S co–doping in the carbon framework significantly enhances both

the rate and cycling performance of soft carbon for service as an anode for LIBs. In addition, other two kinds of nano–$CaCO_3$ particles (The diameters are around 15–30 nm and 60–80 nm) are selected to optimize the pore parameters of NPSC. The as–obtained 30–NPSC and 80–NPSC show a large number of pores around 30 and 80 nm (Fig. S11), respectively. However, 30–NPSC and 80–NPSC can only deliver low capacity of 350 mA h g^{-1} and 320 mA h g^{-1} at 0.5 A g^{-1} after 200 cycles (Fig. S12) which are lower than that of NPSC, thus we believe the opportune pore structure on rate performance of anodes play a key role.

Electrochemical impedance spectroscopy (EIS) measurements after 100 cycles in the fully charged state were then conducted under an open circuit condition from 100 kHz to 10 MHz and the results are shown as Nyquist plots in Fig. S13. The Nyquist plots of the electrodes can be fitted and analyzed well based on the equivalent electric circuit model (inset of Fig. S13). They mainly consist of an indistinct semicircle in the high–frequency region deriving from the migration resistance R_f of Li^+ past the SEI layer and non–ideal capacitance of the SEI (CPE_1), a large semicircle in the middle–frequency region ascribed to charge transfer resistance (R_{ct}) and non–ideal double–layer capacitance (CPE_2), and a sloping line in the low–frequency range corresponding to Warburg diffusion resistance (Z_w) which is related to the Li–ion diffusion in the bulk electrode. In the equivalent circuit, R_e is the ohm internal resistance, including resistances of leads, inter– and outer–cell contacts, electrolyte and electrode bulk resistances; the value is the intercept on the real impedance axis at the high–frequency intersection [42]. Generally, the more vertical the straight line is, the more rapid the ion transport is, which is beneficial for improving the electrochemical capability [43]. Obviously, both the R_f and R_{ct} values are minimum and show relatively more vertical straight line for the NPSC anode (Table S9). This means that NPSC shows the lowest resistance against diffusion of Li ions. NPSC's lower resistance for charge transfer and diffusion is in accordance with its excellent cycling and rate performance.

Further, to explore the feasibility of the as–prepared anode material, the NPSC anode matched with a $LiVPO_4F$ cathode was fabricated into full cells. The $LiVPO_4F$ delivers a stable capacity of 144 mA h g^{-1} in half cells at 30 mA g^{-1} (Fig. 4(a)). The active weight ratio between $LiVPO_4F$ and NPSC is optimized to be 5:1. Fig. 4(b) shows the charge/discharge curves of the full cells; a reversible capacity of 353 mA h g^{-1} (based on the weight of anode) can be achieved at 0.1 A g^{-1} in the voltage window of 1.5–4.2

V. In addition, the full cell reveals excellent cycling stability with 88.6% capacity retention even after 100 cycles, as shown in Fig. 4(c). $LiVPO_4F$||NC, $LiVPO_4F$||NPC and $LiVPO_4F$||NSC cells produced a specific capacity of 80 mA h g^{-1}, 180 mA h g^{-1} and 220 mA h g^{-1}, respectively (Fig. S14a–c). These results can be correlated to the synergistic doping effect and 3D interconnected porous structures.

To further confirm the synergistic effect on the lithium storage performance, first‐principle computations were performed to investigate the adsorption energy of Li atoms on various heteroatom–doped soft carbons. The types of N doping (pyridinic–N), N, S doping (pyridinic–N and thiophene–S), and N, P, S doping (pyridinic–N, thiophene–S and P–S) in graphene were modeled to calculate the adsorption energy of a single Li atom on the hollow heteroatom doping sites of graphene, respectively (Fig. 5). The most stable structures for lithium ion adsorption were optimized. The binding energy between Li and NC, NSC and NPSC was calculated to be −3.66 eV, −3.33 eV and −4.02 eV, respectively, indicating a stronger interaction between Li and NPSC, which is in accordance with the electrochemical performance results in Fig. 3. However, DFT calculation results show a lower adsorption energy of Li^+ with additional S doping compared with that of N doping alone, while the electrochemical performance of NSC is higher than that of NC in lithium storage. Obviously, the diffusion coefficient of Li^+ plays an equally important role to the adsorption energy of Li for anode materials in lithium storage [44]. Compared with NC, NSC shows higher diffusion coefficients during the lithiation and delithiation processes, due to its larger interlayer distance and more active sites. Thus, tuning the adsorption energy of Li and diffusion coefficient of Li^+ via the synergistic doping effect is revealed to be a promising approach to optimization of the electrochemical performance of carbonaceous materials.

Conclusions

N, P and S ternary–doped hierarchical porous soft carbon, with a high concentration of C–S bonds has been prepared though a rational strategy. We have found that the additional introduction of P promotes the incorporation of sulfur into carbon rings in C–S configurations, enhancing the electrochemical activities of the soft carbon. The larger interlayer spacing created by the large heteroatom radius and the hierarchical interconnected porous structures, ensure short transmission paths and enhanced reaction kinetics for Li^+. Benefiting from the synergistic doping effect, the prepared NPSC

electrode shows high reversible specific capacities of 770 mA h g^{-1} at 100 mA g^{-1} and excellent cycling stability with a capacity of 500 mA h g^{-1} after 500 cycles at 500 mA g^{-1} in LIBs. The $LiVPO_4F$/NPSC full cell delivers high discharge capacity (353 mA h g^{-1} at 0.1 A g^{-1}) and superior cycling stability with capacity retention of ~88.6% even after 100 cycles. This outstanding performance demonstrates that the synergistic doping effect can be applied to traditional carbon materials to enhance their electrochemical properties as electrode materials.

Acknowledgements

Financial support is from National Natural Science Foundation of China (No. 51472186).

Competing interests

The authors declare no competing financial interests.

References

[1] B. Obama, Science 355 (2017) aam6284.
[2] D. Larcher, J.M. Tarascon, Nat. Chem. 7 (2014) 19.
[3] M. Armand, J.M. Tarascon, Nature 451 (2008) 652.
[4] L. Fan, Q. Liu, S. Chen, Z. Xu, B. Lu, Adv. Energy Mater. 7 (2017) 1602778.
[5] Z. Jian, C. Bommier, L. Luo, Z. Li, W. Wang, C. Wang, P.A. Greaney, X. Ji, Chem. Mater. 29 (2017) 2314–2320.
[6] Z. Jian, S. Hwang, Z. Li, A.S. Hernandez, X. Wang, Z. Xing, D. Su, X. Ji, Adv. Funct. Mater. 27 (2017) 1700324.
[7] N. Kobayashi, Y. Inden, M. Endo, J. Power Sources 326 (2016) 235–241.
[8] J.P. Paraknowitsch, A. Thomas, Energy Environ. Sci. 6 (2013) 2839–2855.
[9] S.S. Munjewar, S.B. Thombre, R.K. Mallick, Ionics 23 (2017) 1–18.
[10] W.J. Lee, J. Lim, O.K. Sang, Small Methods 1 (2017) 1600014.
[11] F. Sun, J. Gao, Y. Yang, Y. Zhu, L. Wang, X. Pi, X. Liu, Z. Qu, S. Wu, Y. Qin, Carbon 109 (2016) 747–754.
[12] D. Xiong, X. Li, Z. Bai, H. Shan, L. Fan, C. Wu, D. Li, S. Lu, ACS Appl. Mater. Interface 9 (2017) 10643–10651.
[13] M. Graglia, J. Pampel, T. Hantke, T.P. Fellinger, D. Esposito, ACS Nano 10 (2016) 4364–4371.
[14] J. Dong, Y. Xue, C. Zhang, Q. Weng, P. Dai, Y. Yang, M. Zhou, C. Li, Q. Cui, X. Kang, C. Tang, Y. Bando, D. Golberg, X. Wang, Adv. Mater. 29 (2017) 1603692.
[15] Y. Qiu, J. Huo, F. Jia, B.H. Shanks, W. Li, J. Mater. Chem. A 4 (2016) 83–95.
[16] J. Xia, K. Jiang, J. Xie, S. Guo, L. Liu, Y. Zhang, S. Nie, Y. Yuan, H. Yan, X. Wang, Chem. Eng. J. 359 (2019) 1244–1251.
[17] X. Yin, W. Sun, L.P. Lv, Y. Wang, Chem. Eng. J. 346 (2018) 376–387.
[18] W. Yan, X. Cao, J. Tian, C. Jin, K. Ke, R. Yang, Carbon 99 (2016) 195–202.
[19] G. Xin, M. Wang, W. Zhang, J. Song, B. Zhang, Electrochim. Acta 291 (2018) 168–176.
[20] M. Khalid, A.M.B. Honorato, E.A. Ticianelli, H. Varela, J. Mater. Chem. A 6 (2018) 12106–12114.
[21] Q. Guo, Y. Ma, T. Chen, Q. Xia, M. Yang, H. Xia, Y. Yu, ACS Nano, 11 (2017) 12658–12667.
[22] J. Yang, X. Zhou, D. Wu, X. Zhao, Z. Zhou, Adv. Mater. 29 (2017) 1604108.
[23] P. Wang, Y. Zhang, Y. Yin, L. Fan, N. Zhang, K. Sun, ACS Appl. Mater. Interface 10 (2018) 11708–11714.
[24] D. Shao, I. Smolianova, D. Tang, L. Zhang, RSC Adv. 7 (2017) 2407–2414.

[25] M. Sevilla, A.B. Fuertes, Micropor. Mesopor. Mat. 158 (2012) 318–323.
[26] Y. Yan, Y.X. Yin, S. Xin, Y.G. Guo, L.J. Wan, Chem. Commun. 48 (2012) 10663–10665.
[27] G. Kresse, J. Hafner, Phys. Rev. B 47 (1993) 558–561.
[28] A. Tkatchenko, M. Scheffler, Phys. Rev. Lett. 102 (2009) 073005.
[29] G. Ning, X. Ma, X. Zhu, Y. Cao, Y. Sun, C. Qi, Z. Fan, Y. Li, X. Zhang, X. Lan, J. Gao, ACS Appl. Mater. Interface 6 (2014) 15950–15958.
[30] J. Fan, S.W. Boettcher, C.K. Tsung, Q. Shi, M. Schierhorn, G.D. Stucky, Chem. Mater. 20 (2008) 909–921.
[31] Z. Wang, Y. Li, X.J. Lv, RSC Adv. 4 (2014) 62673–62677.
[32] B. Cao, H. Liu, B. Xu, Y. Lei, X. Chen, H. Song, J. Mater. Chem. A 4 (2016) 6472–6478.
[33] A.L.M. Reddy, A. Srivastava, S.R. Gowda, H. Gullapalli, M. Dubey, P.M. Ajayan, ACS Nano 4 (2010) 6337–6342.
[34] N. Liu, L. Yin, C. Wang, L. Zhang, N. Lun, D. Xiang, Y. Qi, R. Gao, Carbon 48 (2010) 3579–3591.
[35] S. Yang, L. Zhi, K. Tang, X. Feng, J. Maier, K. Müllen, Adv. Funct. Mater. 22 (2012) 3634–3640.
[36] Q. Liang, Y. Zheng, C. Du, Y. Luo, J. Zhang, B. Li, Y. Zong, Q. Yan, Small Methods 1 (2017) 1700304.
[37] E.H. Kim, Y. Jung, Carbon Lett. 15 (2014) 277–281.
[38] M.J. Kim, J.T. Yeon, K. Hong, S.I. Lee, N.S. Choi, S.S. Kim, B. Korean Chem. Soc. 34 (2013) 2029–2035.
[39] V. Selvamani, R. Ravikumar, V. Suryanarayanan, D. Velayutham, S. Gopukumar, Electrochim. Acta 190 (2016) 337–345.
[40] L. Wu, D. Buchholz, C. Vaalma, G.A. Giffin, S. Passerini, Chemelectrochem 3 (2016) 292–298.
[41] J.R. Dahn, T. Zheng, Y. Liu, J.S. Xue, Science 270 (1995) 590.
[42] A.A. AbdelHamid, X. Yang, J. Yang, X. Chen, J.Y. Ying, Nano Energy 26 (2016) 425–437.
[43] J. Wang, J. Polleux, J. Lim, B. Dunn, J. Phys. Chem. C 111 (2007) 14925–14931.
[44] H. He, D. Huang, Y. Tang, Q. Wang, X.B. Ji, H.Y. Wang, Z.P. Guo, Nano Energy 57 (2019) 728–736.

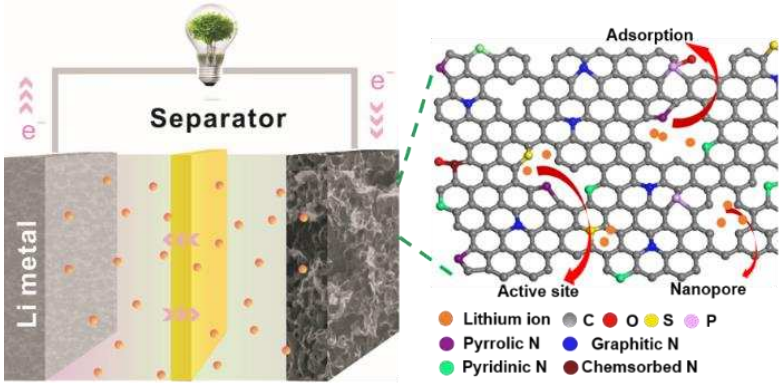

Scheme 1. Schematic illustration of lithium intercalation in hierarchical porous soft carbon with homogeneous doping.

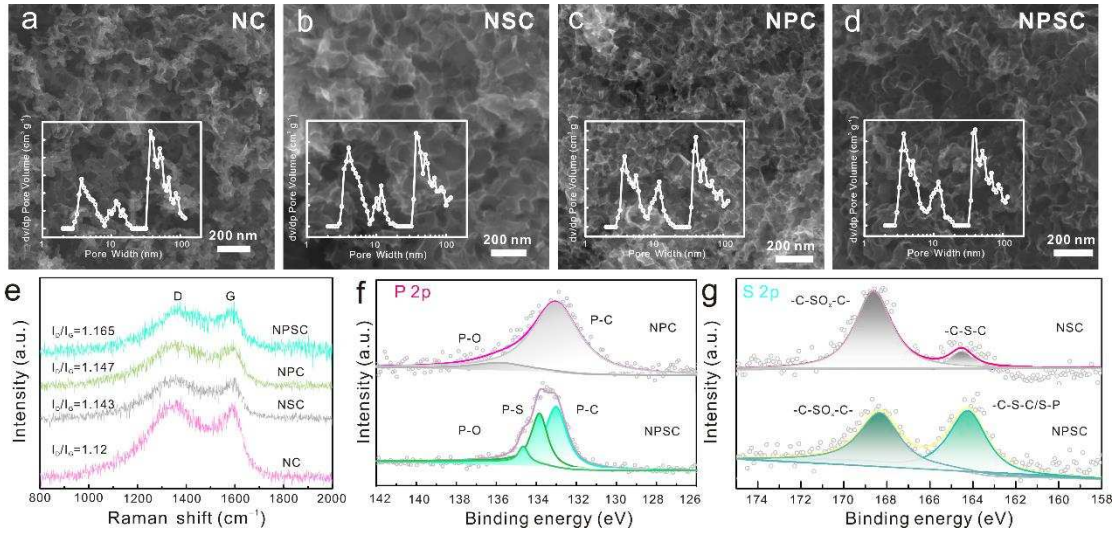

Fig. 1. SEM images of (a) NC, (b) NSC, (c) NPC, and (d) NPSC (inset is the pore size distribution), (e) Raman spectra of the NPSC, NPC, NSC and NC, and the calculated I_D/I_G values are also presented, (f) P–O, P–S and P–C for XPS–P 2p of NPC and NPSC, (g) sulphide (–C–S–C–/S–P) and sulphone (–C–SO_x–C–) for XPS–S 2p of NSC and NPSC.

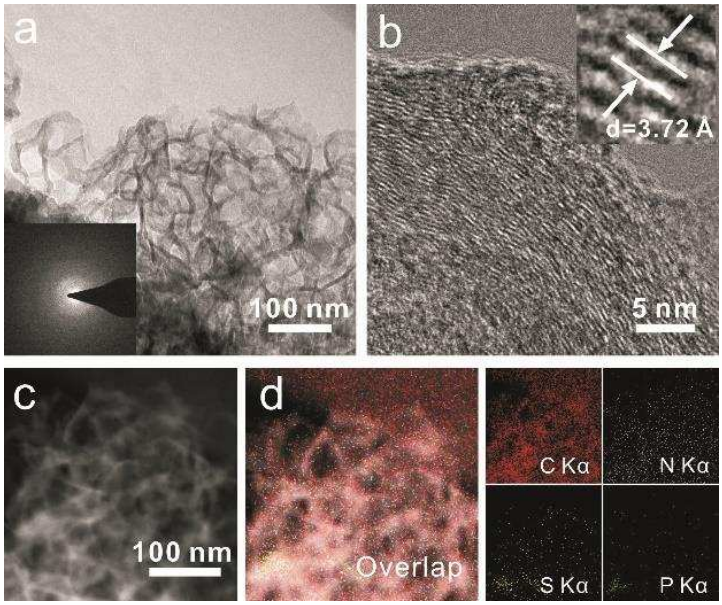

Fig. 2. (a) TEM and (b) HRTEM images of NPSC, inset in (a) is a SAED pattern from the area shown in (a), (c) image and (d) corresponding overlap map of C/N/P/S maps combined, as well as corresponding C, N, P and S elemental mapping images of NPSC.

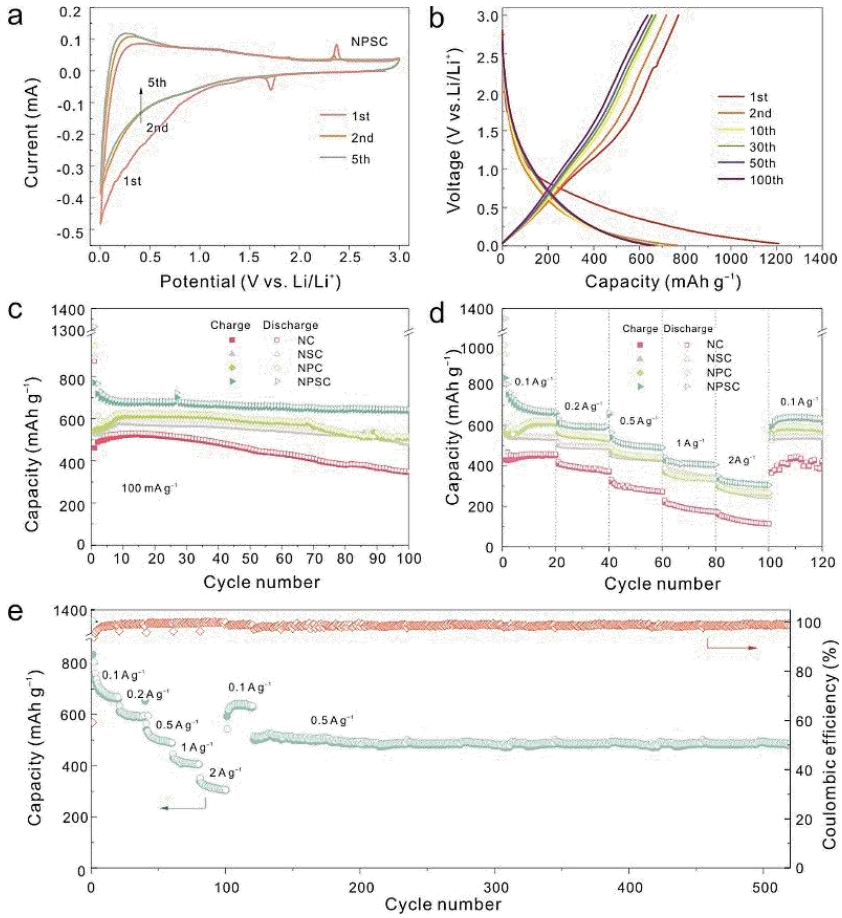

Fig. 3. (a) The voltammetry of the NPSC in the first five cycles between 0.05 and 3.00 V at 0.1 mV s^{-1}; (b) typical galvanostatic charge/discharge profiles with a current density of 100 mA g^{-1}; (c) cycling performance of the prepared electrodes tested in a half–cell at 100 mA g^{-1}; (d) rate performance of NPSC, NPC, NSC and NC electrodes between 100 mA g^{-1} and 2000 mA g^{-1}; (e) prolonged cycle life of NPSC at 500 mA g^{-1}.

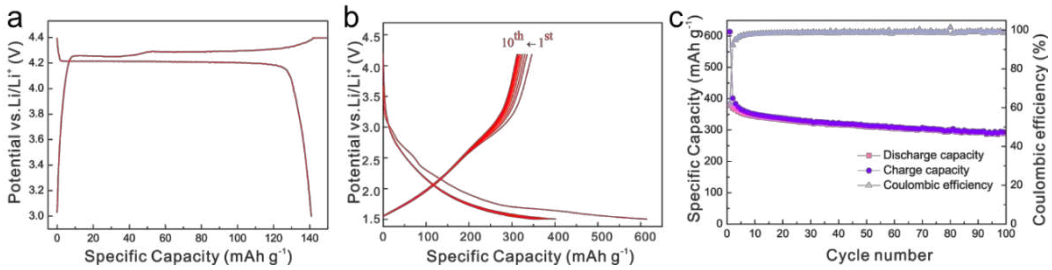

Fig. 4. (a) Typical galvanostatic charge/discharge profiles of $LiVPO_4F$ with a current density of 30 mA g^{-1}, (b) galvanostatic charge/discharge voltage profiles and (c) cycling stability of the $LiVPO_4F$/NPSC full cell at a current density of 100 mA g^{-1}.

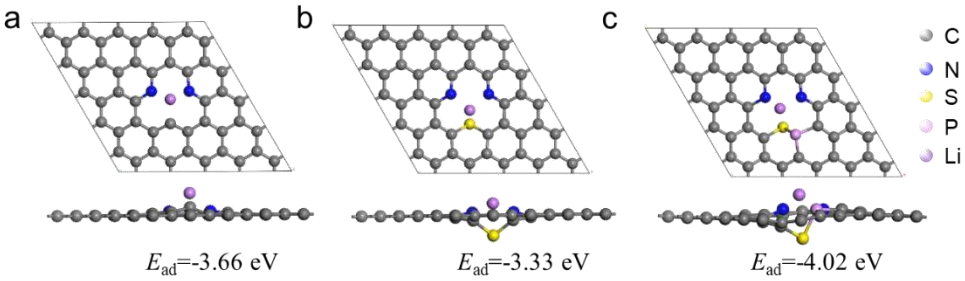

Fig. 5. The configurations of lithium adsorption on (a) NC, (b) NSC and (c) NPSC.